


**Timescale distributions of spin fluctuations in the  $S = 2$  kagome antiferromagnet  $\text{CsMn}_3\text{F}_6(\text{SeO}_3)_2$** Suheon Lee<sup>1,\*</sup>, Tianyu Zhu<sup>2,\*</sup>, Y. Oshima<sup>3</sup>, T. Shiroka<sup>4</sup>, C. Wang<sup>4</sup>, H. Luetkens<sup>4</sup>,  
Haoming Yang<sup>2</sup>, Minfeng Lü<sup>2,†</sup> and K.-Y. Choi<sup>5,‡</sup><sup>1</sup>Center for Integrated Nanostructure Physics, Institute for Basic Science, Suwon 16419, Republic of Korea<sup>2</sup>School of Environmental and Chemical Engineering, Jiangsu University of Science and Technology, Zhenjiang 212003 Jiangsu, China<sup>3</sup>Meson Science Laboratory, RIKEN Cluster for Pioneering Research, Hirosawa 2-1, Wako, Saitama 351-0198, Japan<sup>4</sup>Laboratory for Muon Spin Spectroscopy, Paul Scherrer Institute, 5232 Villigen, Switzerland<sup>5</sup>Department of Physics, Sungkyunkwan University, Suwon 16419, Republic of Korea (Received 5 November 2021; revised 4 March 2022; accepted 4 March 2022; published 29 March 2022)

We report the static and dynamical properties of a newly discovered  $S = 2$  kagome antiferromagnet  $\text{CsMn}_3\text{F}_6(\text{SeO}_3)_2$ . By combining dc and ac magnetic susceptibilities, specific heat, electron spin resonance (ESR), and muon spin relaxation ( $\mu\text{SR}$ ), we identify two characteristic temperatures  $T^* = 8$  K and  $T = |\Theta_{\text{CW}}| = 49(1)$  K, thereby three distinct regimes: a paramagnetic, a cooperative paramagnetic, and a quasistatic ordered state. At high temperature ( $T > |\Theta_{\text{CW}}|$ ), the ac susceptibility and ESR linewidth show a power-law dependence, reflecting short-range spin-spin correlations of the paramagnetic  $\text{Mn}^{3+}$  ions. In the cooperative paramagnetic regime ( $T^* < T < |\Theta_{\text{CW}}|$ ), the ESR signals evince the development of dichotomic spin correlations, which is interpreted in terms of the distinct timescales of in-plane and out-of-plane spin fluctuations. Remarkably, we observe a broad maximum at the characteristic temperature scale of  $T_{\text{cl}} = 20$  K ( $\approx |J_{\text{cl}}|$ ) in the specific heat and ESR results, suggesting short-range ordering. At low temperatures below  $T^*$ , the  $\mu\text{SR}$  data suggest the presence of dynamically fluctuating fields with partially frozen moments, consistent with the absence of long-range order evidenced by specific heat and magnetic susceptibility data. A magnetic behavior that depends on the chosen time window points to the presence of multiple timescales and temporally anisotropic spin correlations, as predicted for a classical kagome antiferromagnet.

DOI: [10.1103/PhysRevB.105.094439](https://doi.org/10.1103/PhysRevB.105.094439)**I. INTRODUCTION**

Two-dimensional kagome antiferromagnets have attracted intense attention in the past decade due to the potential for realizing exotic states of matter, including quantum spin liquid (QSL), quantum kagome ice, and fractionalized excitations [1–4]. Specifically, QSL represents a highly entangled quantum state featuring strong and temporal spin correlations in the absence of long-range magnetic ordering [2,5]. A QSL state is believed to emerge in spin systems with low dimensionality, small spin number, and low coordination number imposed by geometrical frustration. In this context, a two-dimensional  $S = 1/2$  kagome antiferromagnet serves as a promising platform to search for QSLs. Nevertheless, intensive efforts have also been made to realize QSL in the kagome systems with a high spin number ( $S > 1/2$ ).

A variety of  $S = 1/2$  kagome family materials showcase fractionalized spin excitations in the absence of long-range ordering, including the herbertsmithite  $\text{ZnCu}_3(\text{OH}_6)\text{Cl}_2$ , the kapellasite  $\text{Cu}_3\text{Zn}(\text{OH}_6)\text{Cl}_2$ , and the Zn-barlowite  $\text{Cu}_3\text{Zn}(\text{OH})_6\text{FBr}$  [4,6–8]. Numerous theoretical studies of the  $S = 1/2$  Heisenberg antiferromagnetic model on a quantum

kagome lattice (KHAFM) reveal that the resonating valence bond, gapped  $Z_2$ , and gapless  $U(1)$  spin liquids are nearly degenerate in the ground-state energies [5]. In the classical limit, the nonlinearity of the KHAFM leads to rich spin dynamics and a plethora of quantum and classical phases [9,10]. At high temperatures [ $T > |J_{\text{cl}}|$ ] with  $J_{\text{cl}} = JS(S + 1)$ , a conventional paramagnet is characterized by short-range spin-spin correlations. In the cooperative paramagnetic regime ( $10^{-2} < T/|J_{\text{cl}}| < 1$ ), spins on each triangular cluster of the kagome lattice form local  $120^\circ$  arrangements, and spin correlations show a dipolar-like decay [11]. When coplanar correlations are well developed in the coplanar regime ( $T/|J_{\text{cl}}| < 10^{-2}$ ), the weather-vane modes are generated by continuous rotations of spins. In addition, a spin nematic or a coplanar ground state emerges through the order-by-disorder mechanism [12–16].

On the experimental side, few kagome compounds with large spin ( $S > 1/2$ ) have been reported so far. The jarosites with  $S = 5/2$ ,  $\text{AFe}_3(\text{OH})_6(\text{SO}_4)_2$  ( $A = \text{Na}, \text{K}, \text{and } \text{H}_3\text{O}$ ), undergo spin-glass transitions at  $T_f = 15$  K for  $A = \text{H}_3\text{O}$  and antiferromagnetic ordering at a temperature of the order of 50 K for  $A = \text{Na}$  and  $\text{K}$  [17,18]. Furthermore, the layered monodiphosphate  $\text{Li}_9\text{Fe}_3(\text{P}_2\text{O}_7)_3(\text{PO}_4)_2$  with  $S = 5/2$  exhibits a thermal crossover from classical spin liquid to antiferromagnetic order through  $T_N = 1.3$  K and a characteristic  $1/3$  magnetization plateau [19]. On the other hand, the  $S = 3/2$  kagome antiferromagnet  $\text{KCr}_3(\text{OH})_6(\text{SO}_4)_2$  undergoes no long-range ordering down to 25 mK [20–22].

\*These authors contributed equally to this work.

†m.f.lv@hotmail.com

‡choisky99@skku.edu

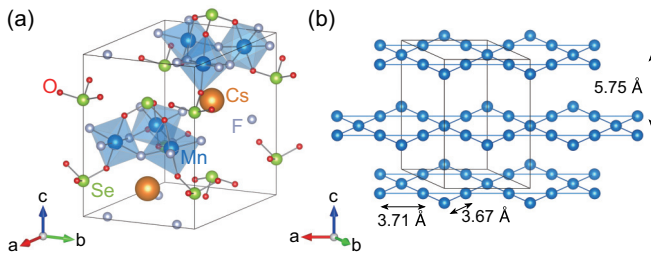


FIG. 1. (a) Crystal structure of  $\text{CsMn}_3\text{F}_6(\text{SeO}_3)_2$ . The orange, blue, green, gray, and red spheres represent the Cs, Mn, Se, F, and O atoms, respectively. The solid line denotes the hexagonal unit cell. The corner-sharing  $\text{MnF}_4\text{O}_2$  octahedra constitute a two-dimensional kagome lattice in the  $ab$ -plane. (b) The kagome lattice of  $\text{Mn}^{3+}$  ions in the  $ab$ -plane, separated by nonmagnetic layers with an interlayer distance 5.75 Å. The tilting of the  $\text{MnF}_4\text{O}_2$  octahedra leads to two slightly different triangular units with the interatomic distances of 3.67 and 3.71 Å. The Cs, Se, F, and O atoms are omitted for clarity.

Nevertheless, due to the scarcity of candidate materials, the dynamical properties of  $S = 2$  kagome systems are not well understood. Here, we introduce  $\text{CsMn}_3\text{F}_6(\text{SeO}_3)_2$ , an  $S = 2$  KHAFM that structurally constitutes a kagome network made of two slightly distinct  $\text{Mn}^{3+}$  equilateral triangles (see Fig. 1).

$\text{CsMn}_3\text{F}_6(\text{SeO}_3)_2$  (CCDC 2112024) crystallizes in the hexagonal structure (space group no. 186,  $P6_3mc$ ) with the lattice constants  $a = 7.3891$  Å and  $c = 11.5009$  Å. As depicted in Fig. 1(a),  $\text{Mn}^{3+}$  ions are surrounded by the  $\text{O}^{2-}$  and  $\text{F}^-$  ions, forming octahedral environments. Each  $\text{MnF}_4\text{O}_2$  octahedron is tilted about  $19^\circ$  from the local  $c$ -axis. The  $S = 2$  Mn spins interact with each other via the Mn-F-Mn superexchange pathway with bond angles of  $135.1^\circ$  and  $136.4^\circ$  in the  $ab$ -plane. As a consequence, the exchange couplings between the Mn spins give rise to two types of equilateral triangular units with different sizes, 3.67 and 3.71 Å for the small and the large bond angles, respectively [see Fig. 1(b)]. Note that the exchange interactions for both units are not much different because of the comparable intratriangle distances. As such, the corner-sharing network of the triangular units realizes the kagome lattices (with a small breathing anisotropy) in the  $ab$ -plane, which are separated by nonmagnetic ions with an interlayer distance of 5.75 Å.

In this work, we combine thermodynamic and resonance techniques to elucidate the static and dynamical properties of the newly discovered  $S = 2$  KHAFM  $\text{CsMn}_3\text{F}_6(\text{SeO}_3)_2$ . The dc magnetic susceptibility and specific-heat data evidence a crossover from a paramagnetic to a cooperative paramagnetic state at the temperature scale of the Curie-Weiss temperature  $\Theta_{\text{CW}} = -49(1)$  K. Further, our electron spin resonance (ESR) and muon spin relaxation ( $\mu\text{SR}$ ) experiments unveil the coexistence of fast dynamics with a spin frozen state and two timescales of spin correlations in the cooperative paramagnetic state, indicative of a timescale distribution of spin correlations.

## II. EXPERIMENTAL DETAILS

Single crystals of  $\text{CsMn}_3\text{F}_6(\text{SeO}_3)_2$  were grown by a hydrothermal method. A mixture of  $\text{MnO}_2$ ,  $\text{SeO}_2$ ,  $\text{CsOH} \cdot \text{H}_2\text{O}$ , HF, deionized water, and solvents was sealed in an autoclave

equipped with a Teflon liner. The autoclave was heated to  $220^\circ\text{C}$  for 72 h and then cooled down to room temperature ( $2.5^\circ\text{C/h}$ ). Tiny crystals were washed with distilled water and then filtered. Single-phase polycrystalline samples were obtained by separating and grinding small pieces of the single crystals.

The crystal structures were solved using a charge flipping method implemented in the SUPERFLIP software [23] and refined using the JANA 2006 program [24] on  $F^2$  with full-matrix least-squares methods. The fluorine atoms as well as oxygen atoms were determined under a similar process and partially reported elsewhere [25–27]. The structural details are described in the Supplemental Material [28].

Magnetic susceptibility and magnetization were measured using a SQUID magnetometer and a vibrating sample magnetometer (Quantum Design MPMS and VSM) up to 7 T in the temperature range of  $T = 2\text{--}300$  K. Specific-heat measurements were carried out using a physical property measurement system (Quantum Design PPMS) in zero field for  $T = 1.6\text{--}300$  K. ESR was measured by a conventional X-band ESR system (JEOL JES-RE3X). The temperature-dependent ESR signals were recorded at  $T = 3.3\text{--}200$  K using a continuous He-flow cryostat (ESR 900, Oxford Instruments).

Zero-field (ZF) and longitudinal-field (LF)  $\mu\text{SR}$  experiments were carried out on the GPS spectrometer using  $^4\text{He}$  cryostat ( $1.6 < T < 200$  K) and the Dolly spectrometer equipped with  $^3\text{He}$  cryostat ( $0.3 < T < 4$  K) at Paul Scherrer Institute (Villigen, Switzerland). The polycrystalline samples of  $\text{CsMn}_3\text{F}_6(\text{SeO}_3)_2$  were mixed with ethanol diluted GE varnish and attached to a Cu plate. To determine the detector efficiency  $\alpha$  between forward and backward positron detectors, on each detector, we performed weak transverse field measurements in an applied field of  $H = 30\text{--}50$  G at high temperatures. The obtained  $\mu\text{SR}$  results were analyzed using the software package MUSRFIT [29]. The temperature-independent background was evaluated to be about 3% of the total asymmetry and subtracted from the raw data. We normalized the corrected asymmetry by the theoretical values from the fittings and plotted the muon spin polarization.

## III. RESULTS

### A. Magnetic susceptibilities and magnetization

Figure 2(a) displays the temperature dependence of the zero-field-cooled (ZFC) and field-cooled (FC) magnetic susceptibility measured in an applied field of 0.5 T. We observe no bifurcation between the ZFC and FC curves down to 2 K, ruling out the possibility of conventional spin glass. With decreasing temperature, the dc magnetic susceptibility  $\chi_{\text{dc}}(T)$  increases steeply in the absence of saturation or anomaly, suggesting a lack of long-range magnetic ordering down to 2 K.

As shown by the green solid lines of Figs. 2(a) and 2(b), the Curie-Weiss (CW) law gives a nice description of  $\chi_{\text{dc}}(T)$  down to 10 K. Fitting to the data yields the Curie constant  $C = 3.093(1)$  emu mol $^{-1}$  Oe $^{-1}$  K Mn $^{-1}$  and the CW temperature  $\Theta_{\text{CW}} = -49.0(1)$  K. The effective magnetic moment is evaluated to be  $\mu_{\text{eff}} = 4.97(9)\mu_{\text{B}}$ , comparable to the spin-only value  $4.90\mu_{\text{B}}$  for the  $\text{Mn}^{3+}$  ions in a high-spin state ( $3d^4$ ,  $S =$

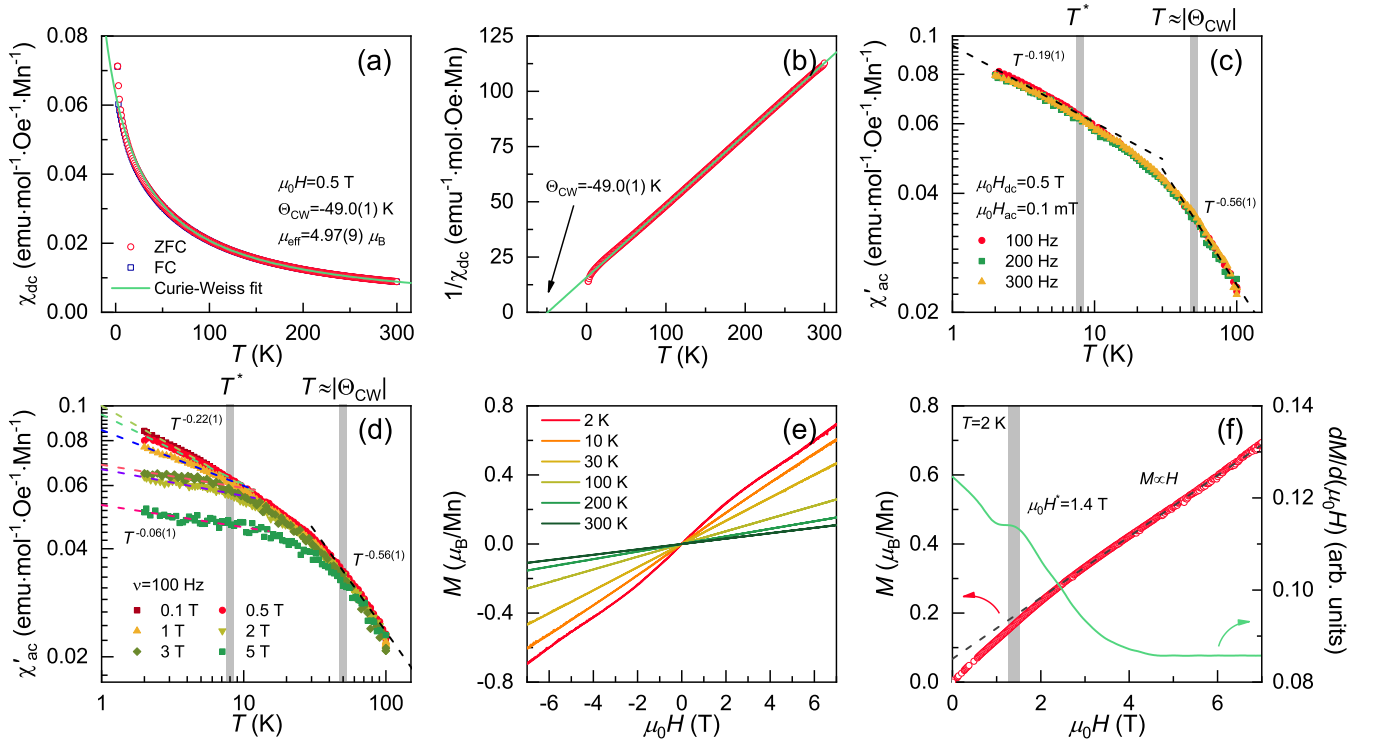


FIG. 2. (a) Temperature dependence of the dc magnetic susceptibility  $\chi_{dc}(T)$  measured in an applied field of 0.5 T. (b) Inverse dc magnetic susceptibility  $1/\chi_{dc}(T)$  as a function of temperature. The solid curves represent the Curie-Weiss fit to the data. (c) Real part of the ac magnetic susceptibility  $\chi'_{ac}(T)$  at various frequencies in a log-log scale. (d) Double logarithmic plot of the field dependence of  $\chi'_{ac}(T)$  measured at the ac frequency  $\nu = 100$  Hz. The dashed lines denote fits to the power law  $\chi'_{ac} \propto T^{-n}$ . The shaded bars denote the characteristic temperatures  $T^* = 8$  K and  $T = |\Theta_{CW}|$ , at which  $\chi'_{ac}(T)$  displays distinct power-law behaviors. (e) Magnetization curves  $M(H)$  measured at different temperatures. (f) Isothermal magnetization at 2 K together with its first derivative with respect to  $H$ . The dashed line indicates a linear increase of  $M(H)$  above 2.2 T. The shaded region indicates a field-induced crossover at  $\mu_0H^* = 1.4$  T, as evidenced by a small hump in  $dM(H, T = 2 \text{ K})/d(\mu_0H)$ .

2). The negative value of  $\Theta_{CW}$  indicates predominant antiferromagnetic exchange interactions. Using  $k_B\Theta_{CW} = 2zS(S+1)J/3$  with  $z = 4$  the nearest-neighbor coordination number of the kagome lattice, the exchange coupling constant is estimated to be  $J = -3.06$  K, alluding to weak antiferromagnetic interactions between the Mn spins. Here, we note that the CW law is valid well below  $|\Theta_{CW}|$ , which is the  $\chi_{dc}$  fingerprint of a cooperative paramagnetic state [30]. We recall that  $|\Theta_{CW}|$  gives a mean-field temperature scale for the onset of a paramagnetic-to-cooperative paramagnetic crossover. The cooperative paramagnetic state featuring short-range correlations in space and time is continuously connected to a high-temperature paramagnetic phase, which is characteristic of classical frustrated magnets (*vide infra*) [30].

We further performed the ac susceptibility measurements at various frequencies and fields. In Figs. 2(c) and 2(d), we plot the real part of the ac magnetic susceptibility  $\chi'_{ac}$  in a log-log scale. We observe no discernible frequency dependence of  $\chi'_{ac}(T)$ , confirming the absence of spin freezing down to 2 K. Noticeably,  $\chi'_{ac}(T)$  shows two distinct power-law regimes at low and high temperatures. Namely,  $\chi'_{ac}(T)$  follows a power-law behavior  $T^{-n}$  with the exponent of  $n = 0.56(1)$  for  $T > |\Theta_{CW}|$  and changes its exponent to  $0.19(1)$  below  $T^* = 8$  K. This signifies that the high-temperature paramagnetic state is governed by short-range spin-spin correlations.

The field dependence of  $\chi'_{ac}(T)$  is depicted in Fig. 2(d). Above  $T = |\Theta_{CW}|$ ,  $\chi'_{ac}(T)$  displays a nearly field-independent behavior, while below  $T^*$ ,  $\chi'_{ac}(T)$  is systematically suppressed in conjunction with the decreasing exponent  $n$  with increasing field. Specifically, at low fields ( $\mu_0H \leq 1$  T), the power-law exponent decreases moderately from  $0.22(1)$  to  $0.15(1)$  with increasing field. On the other hand, the exponent  $n$  hardly varies with increasing field,  $n = 0.06(1) - 0.07(1)$  for  $\mu_0H \geq 2$  T. The distinct field dependence through 1 T may be related to the field-induced change of spin correlations, as indicated by the magnetization at 2 K [see Fig. 2(f)].

Isothermal magnetization  $M(H, T)$  measured at different temperatures is presented in Fig. 2(e). We observe no hysteric behavior down to 2 K, precluding ferromagnetic correlations. With increasing temperature,  $M(H, T)$  systematically decreases. To take a close look, we zoom the isothermal magnetization at 2 K in Fig. 2(f).  $M(H, T = 2 \text{ K})$  deviates from a linear extrapolation below 2 T. While the linear increment of  $M(H)$  is typically expected for an antiferromagnetic system, the slope change would be involved with a field-induced change of magnetic correlations in the absence of long-range magnetic order. To determine the anomaly field, we take the first derivative of the isothermal magnetization with respect to the applied field  $dM(H, T = 2 \text{ K})/d(\mu_0H)$ . As shown in Fig. 2(f),  $dM(H, T = 2 \text{ K})/d(\mu_0H)$  reveals

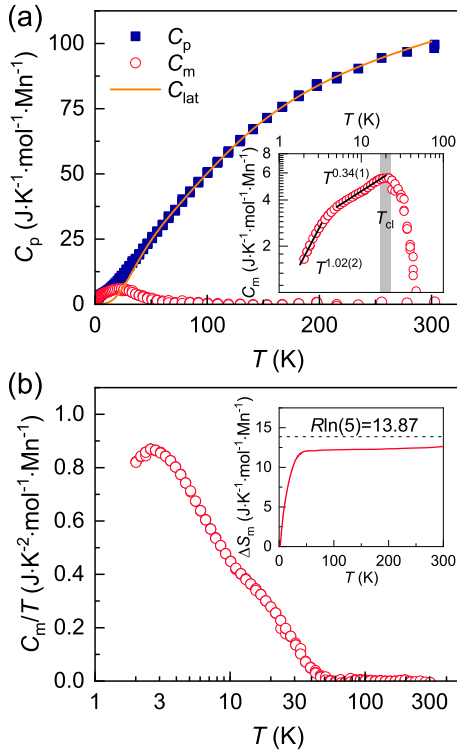


FIG. 3. (a) Total specific heat as a function temperature  $C_p(T)$ . The lattice contribution to the specific heat  $C_{\text{lat}}(T)$  is calculated using the sum of one Debye and two Einstein models, as described in the main text, and is plotted as the orange solid curve. The magnetic specific heat  $C_m(T)$  is obtained by subtracting  $C_{\text{lat}}(T)$  from  $C_p(T)$ . The inset displays the magnetic specific heat as a function of temperature for  $T = 1$ –100 K in a log-log scale. The solid lines indicate power-law behaviors. The shaded bar represents the broad maximum temperature  $T_{\text{cl}} = 20$  K. (b) Temperature dependence of the magnetic specific heat divided by temperature  $C_m(T)/T$ . The inset shows the calculated magnetic entropy  $\Delta S_m$  by integrating  $C_m(T)/T$ . The dashed line represents the theoretically expected value  $R \ln(5) = 13.87 \text{ J K}^{-1} \text{ mol}^{-1} \text{ Mn}^{-1}$  for  $S = 2$ .

a hump at  $\mu_0 H^* = 1.4$  T, indicating the occurrence of a field-induced crossover. Before proceeding, we comment that recent theoretical studies have proposed that kagome-lattice antiferromagnets ( $S > 1/2$ ) entail the so-called *uud* state, showing a magnetization plateau at one-third of the saturation magnetization [31,32]. Indeed, the  $1/3$  magnetization plateau is observed in the  $S = 5/2$  KHAFM  $\text{Li}_9\text{Fe}_3(\text{P}_2\text{O}_7)_3(\text{PO}_4)_2$  [19]. As such, for the studied compound, we expect the one-third magnetization plateau around 20 T, which can be tested by future high-field magnetization experiments.

### B. Specific heat

The temperature dependence of the specific heat  $C_p(T)$  is plotted in Fig. 3(a). We observe no apparent  $\lambda$ -like anomaly or cusp, rendering long-range ordering down to 1.6 K improbable. To single out the magnetic contributions  $C_m(T)$  from the total  $C_p(T)$ , we estimate the lattice contribution based on the

sum of one Debye and two Einstein functions above 50 K as

$$C_{\text{lat}}(T) = 9C_D N k_B \left(\frac{T}{\theta_D}\right)^3 \int_0^{\theta_D/T} \frac{x^4 e^x}{(e^x - 1)^2} dx + 3N k_B \sum_{i=1,2} C_E^i \left(\frac{\theta_E^i}{T}\right)^2 \frac{e^{(\theta_E^i/T)}}{(e^{(\theta_E^i/T)} - 1)^2}. \quad (1)$$

Here,  $C_D$  and  $C_E^i$  are the weighting factors,  $k_B$  is the Boltzmann constant, and  $\theta_D$  ( $\theta_E^i$ ) is the Debye (Einstein) temperature. For the fittings, the sum of the weighting factors was fixed to match the total number of atoms per formula unit divided by the number of Mn ions ( $C_D + C_E^1 + C_E^2 = 18/3 = 6$ ). The fitting parameters are evaluated to be  $\theta_D = 205(1)$ ,  $\theta_E^1 = 521(7)$ ,  $\theta_E^2 = 1801(47)$ ,  $C_D = 2.0(5)$ ,  $C_E^1 = 2.5(3)$ , and  $C_E^2 = 1.5(3)$ . The obtained values are comparable to those of other kagome family compounds  $\text{PbCu}_3\text{TeO}_7$  and  $\text{SrCuTeO}_6$  [33,34].

As shown in Fig. 3(a), the estimated lattice contributions  $C_{\text{lat}}(T)$  well reproduce the high- $T$  behavior of  $C_p(T)$ . By subtracting  $C_{\text{lat}}(T)$  from  $C_p(T)$ , we obtain the magnetic specific heat  $C_m(T)$ . As the temperature is lowered,  $C_m(T)$  begins to increase below 50 K and shows a broad maximum at  $T_{\text{cl}} = 20$  K [see the inset of Fig. 3(a)]. The onset and the broad maximum temperatures coincide with the CW temperature and the temperature scale  $|J_{\text{cl}}| = |J|S(S+1) = 18$  K evaluated from the dc and ac susceptibilities [see Figs. 2(a)–2(d)]. The  $C_m(T)$  data corroborate the entrance to a cooperative paramagnetic (classical spin-liquid) state through  $T = |\Theta_{\text{CW}}|$  and the short-range ordering at  $T_{\text{cl}} = 20$  K ( $\approx |J_{\text{cl}}|$ ).

Upon further cooling, the magnetic specific heat shows two distinct power-law behaviors  $C_m(T) \propto T^n$ . The exponential changes from  $n = 0.34(1)$  to  $1.02(2)$  through 3.5–4.5 K. Generally, the  $T$  linear dependence is regarded as evidence for the low- $E$  gapless excitations in frustrated magnets [35]. However, a limited temperature window of our  $C_m(T)$  data disallows proving the presence of gapless fractionalized excitations, deserving further investigation. From a semilog plot of  $C_m(T)/T$  versus  $T$ , we identify a broad maximum at 2.7 K without any sharp anomaly in addition to the  $T_{\text{cl}} = 20$  K maximum of  $C_m(T)$  pertaining to the short-range ordering. The small peak in  $C_m(T)/T$  alone should not be regarded as true long-range ordering because it is observed in highly frustrated kagome spin systems, ranging from QSLs, exotic  $\mathbf{q} = \mathbf{0}$  pinwheel magnetic order, and three-dimensional long-range order [36–38].

By integrating  $C_m(T)/T$ , the magnetic entropy  $\Delta S_m(T)$  is calculated as shown in the inset of Fig. 3(b).  $\Delta S_m(T)$  exhibits the saturation to  $12.65 \text{ J K}^{-2} \text{ mol}^{-1} \text{ Mn}^{-1}$ , which is close to the theoretically expected value  $R \ln(2S+1) = 13.87 \text{ J K}^{-2} \text{ mol}^{-1} \text{ Mn}^{-1}$  for  $S = 2$ . A missing magnetic entropy ( $\sim 8.7\%$ ) suggests the possibility for magnetic ordering at lower temperatures below 0.3 K (from the  $\mu\text{SR}$  data) or an overestimation of the lattice contribution  $C_p(T)$ . With decreasing temperature below 50 K, the magnetic entropy is gradually released by the enhanced spin correlations. Noticeably, only 3.5% of  $\Delta S_m(T)$  is released below 2.7 K, imposing a constraint to a very weak magnetic order, if present.

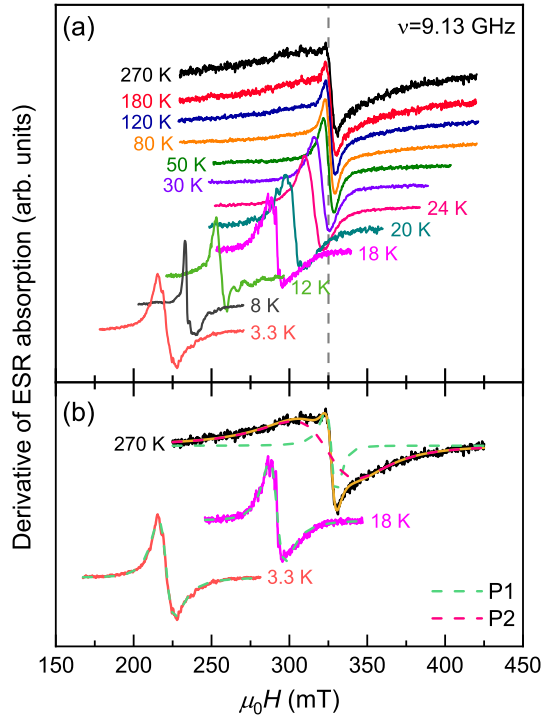


FIG. 4. (a) Temperature dependence of the derivative of ESR absorption. The ESR spectra are vertically shifted for clarity. The dashed vertical line indicates the reference field for  $g = 2$ . (b) Representative ESR spectra at selected temperatures  $T = 3.3, 18$ , and  $300$  K together with theoretical curves. The solid curves represent fits to the data using two (one) Lorentzian profiles above (below)  $30$  K. The dashed lines correspond to the fitted sharp and broad signals, which are labeled as P1 and P2, respectively.

### C. Electron spin resonance

To shine a light on spin fluctuations and spin correlations inherent to a classical kagome antiferromagnet, we turn to the ESR results measured at  $\nu = 9.13$  GHz. Figure 4 shows the temperature dependence of the X-band ESR spectra. In the high-temperature paramagnetic state, the powder ESR spectrum consists of two Lorentzian profiles. The Lorentzian line shape means that the ESR linewidth is dictated by the exchange-narrowing mechanism. On cooling through  $30$  K, the broad line (P2) vanishes while the narrow line (P1) is observed over the whole measured temperature [see Fig. 4(b)]. Based on the disparate temperature dependence, we infer that P1 and P2 are related to out-of-plane and in-plane spin correlations. For unambiguous assignment, a single-crystal study is desired. The  $g$  values are  $g_{P1} = 1.99(8)$  and  $g_{P2} = 1.99(4)$  at  $T = 270$  K, which are typical for the high-spin configuration of  $\text{Mn}^{3+}$  having a less than half-filled shell. The peak-to-peak linewidths are given by  $\Delta H_{pp}^{P1} = 6.82(5)$  mT and  $\Delta H_{pp}^{P2} = 40.35(2)$  mT.

Figure 5 plots the temperature dependence of  $\Delta H_{pp}$  and the resonance field  $H_{res}$  ( $g$ -value). We observe a distinct temperature evolution of the ESR parameters. With lowering temperature below  $150$  K, the broad line displays a weak power-law broadening  $\Delta H_{pp}^{P2}(T) \sim T^{-0.25(2)}$  and then a critical-like broadening  $\Delta H_{pp}^{P2}(T) \sim T^{-1.32(1)}$  through  $T =$

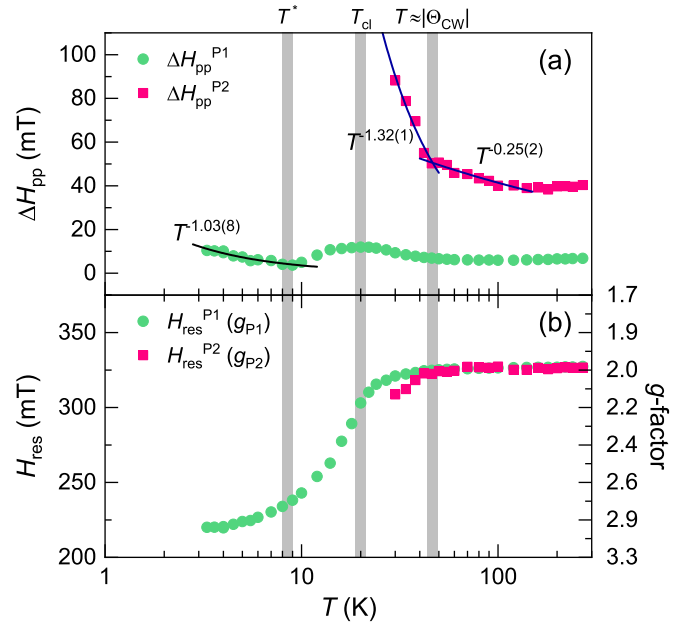


FIG. 5. (a) Temperature dependence of the peak-to-peak linewidth  $\Delta H_{pp}(T)$  for both P1 and P2 in a semilog scale. The solid lines denote fits to the data using the power law  $\Delta H_{pp} \propto T^{-n}$ . The shaded vertical lines indicate the three characteristic temperatures  $T^*$ ,  $T_{cl}$ , and  $|\Theta_{CW}|$ . (b) The resonance fields  $H_{res}(T)$  as a function of temperature in a linear-log scale.

$|\Theta_{CW}|$  and finally a wipe-out below  $30$  K. Remarkably, the exponent change accompanies the crossover between the high- $T$  paramagnetic and the cooperative paramagnetic crossover states, and the wipeout effect occurs at the short-range-ordering temperature inferred from the  $C_m(T)$  data. On the other hand,  $\Delta H_{pp}^{P1}(T)$  of the narrow line bears a resemblance with  $C_m(T)$  except for the power-law broadening  $\Delta H_{pp}^{P1}(T) \sim T^{-1.03(8)}$  below  $T^* = 8$  K [compare the inset of Fig. 3(a) with the P1 symbols in Fig. 5(a)].  $\Delta H_{pp}^{P1}(T)$  is largely temperature-independent for  $T > |\Theta_{CW}|$  and shows a maximum around  $T_{cl} = 20$  K.  $H_{res}$  for both directions starts to shift to lower fields for temperatures below  $T = |\Theta_{CW}|$ , reflecting the buildup of local internal magnetic fields.

Interestingly,  $\Delta H_{pp}^{P1}(T)$  and  $C_m(T)$  show a similar thermal evolution. Given that the magnetic specific heat and the ESR linewidth are related to low-lying magnetic excitations and the spin-spin relaxation rate of electron spins, respectively, a direct relation is lacking between the two quantities. Nonetheless, we cannot totally exclude the possibility that the spin-spin relaxation rate is largely determined by the dynamics of the low-energy excitations inherent to  $S = 2$  KHAMF.

The salient feature of our ESR data probing magnetic correlations on the GHz timescale is the presence of two types of spin correlations. The disparate thermal evolution of the P1 and P2 lines with largely different linewidths is hardly explained within a single timescale of spin fluctuations. More concretely, the narrow P1 line emulates the static thermodynamic behavior, while the broad P2 line is sensitive to the development of local spin correlations. The narrow line should not be ascribed to orphan spins because

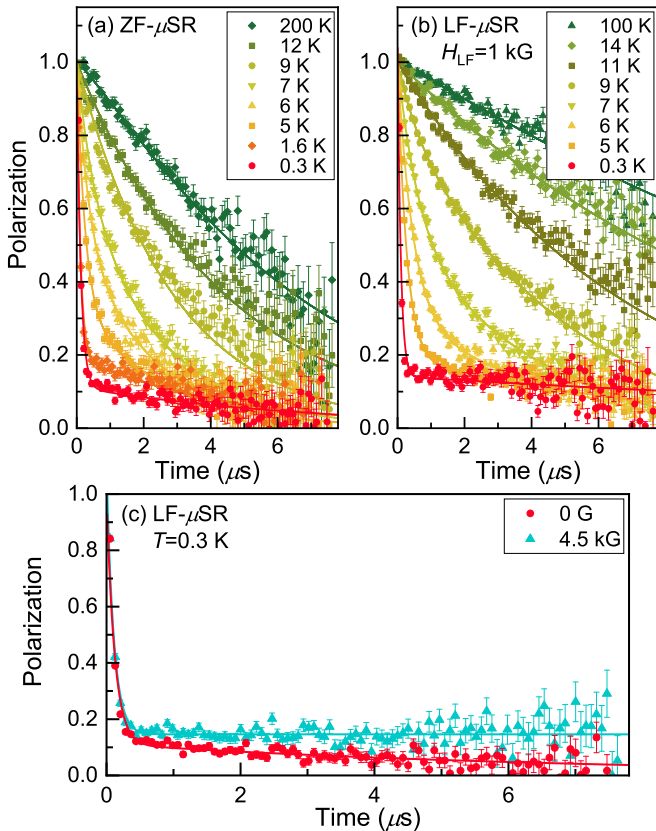


FIG. 6. Representative (a) ZF- and (b) LF- $\mu$ SR spectra at different temperatures. The solid curves represent fits to the data using the sum of two exponential functions as described in the main text. (c)  $\mu$ SR spectra at 0.3 K measured in the zero field and the applied LF of 4.5 kG. The solid curves denote fits to the data, as described in the main text.

its  $g$ -factor deviates from  $g = 2$  at low temperatures and its intensity does not show a Curie-like growth with decreasing temperature. In addition, unlike the diluted Cr-based breathing pyrochlore  $\text{LiGa}_{1-x}\text{In}_x\text{Cr}_4\text{O}_8$ , the dichotomy of magnetic correlations in  $\text{CsMn}_3\text{F}_6(\text{SeO}_3)_2$  is not due to the existence of two magnetic subsystems [39]. Rather, the distinct thermal evolution of the P1 and P2 lines signifies two timescales associated with out-of-plane and in-plane spin correlations, respectively, consistent with the theoretically predicted distribution of timescales in the cooperative paramagnetic regime [16]. Therefore, these observations should be regarded as the precursor of strong temporally anisotropic spin correlations inherent to the coplanar dynamical regime of a classical KHAFM at lower temperatures.

#### D. Muon spin relaxation

To determine the magnetic ground state and the thermal evolution of spin correlations, we conducted ZF- and LF- $\mu$ SR experiments down to  $T = 0.3$  K.

As shown in Fig. 6(a), the high-temperature ZF- $\mu$ SR spectra show an exponential decay, as expected for the rapidly fluctuating fields of paramagnetic spins. With decreasing temperature below 20 K, the muon spin relaxation becomes faster

by the development of spin correlations. Upon cooling below  $T^* = 8$  K, most of the muon spins depolarize within a short timescale ( $< 2 \mu\text{s}$ ). Remarkably, at the lowest measured temperature 0.3 K, 90% of the muon spin polarization decays within the timescale of  $0.5 \mu\text{s}$  with no obvious indications for long-range magnetic ordering, such as coherent muon spin oscillations or a  $1/3$ -recovery of the long-time polarization [40]. The rapidly decaying polarization at short times suggests the presence of quasistatic magnetic moments, while the slow relaxation reflects dynamically fluctuating magnetic moments.

It should be noted that we detect no muon spin precessions stemming from  $\mu^+ - \text{F}^-$  dipolar interactions. Often, the halide materials, containing  $\text{F}^-$ ,  $\text{Cl}^-$ , or  $\text{Br}^-$  ions, feature a coherent oscillation signal due to the dipolar interactions in zero field, as reported in a range of kagome antiferromagnets [6,7,37,41]. For  $\text{CsMn}_3\text{F}_6(\text{SeO}_3)_2$ , however, we find no oscillations arising from  $\mu^+ - \text{F}^-$  couplings. One plausible scenario is that local fields at the muon stopping sites induced by the Mn moments are stronger than the dipolar fields from the F nuclei due to the large magnetic moment of the Mn ions. Similarly, also the  $\text{LiMPO}_4$  ( $M = \text{Mn, Fe, Co, Ni}$ ) compounds do not show  $\mu^+ - \text{F}^-$  dipolar oscillations [42]. The other scenario is that most of the implanted muons might be preferentially located near the apical  $\text{O}^{2-}$  sites rather than close to the  $\text{F}^-$  ions [see Fig. 1(a)].

Figure 6(b) exhibits the temperature dependence of the LF- $\mu$ SR spectra measured in an applied LF of 1 kG. The application of the LF decouples the Mn spins from the nuclear contribution to the muon spin depolarization in the material. Above 10 K, the muon spin polarization is somewhat recovered by the applied LF, compared to the ZF data. However, for  $T < 5$  K, only the slow relaxation component shows a systematic recovery at long times ( $t > 0.5 \mu\text{s}$ ) with increasing  $H_{\text{LF}}$  up to 4.5 kG [see also Fig. 6(c)]. This implies that, at low temperatures, the applied LF hardly decouples the muon spins from the internal local fields, indicating that the dynamically fluctuating fields are predominant in the time window of the  $\mu$ SR technique ( $\sim \text{MHz}$ ). These observations are consistent with the lack of a long-range-ordered state based on our thermodynamic data. The  $\mu$ SR results, including the rapidly relaxing muon spin depolarization and its undecouplable behavior, suggest that the ground state of  $\text{CsMn}_3\text{F}_6(\text{SeO}_3)_2$  has a dynamic nature entailing a fraction of frozen moments, being close to a quasistatic ground state [37,43].

For a quantitative analysis, we fit the data using the sum of two exponential functions,  $P_z(t) = a_{\text{fast}} \exp[-\lambda_{\text{f}} t] + (1 - a_{\text{fast}}) \exp[-\lambda_{\text{s}} t]$ . The obtained fit parameters are summarized in Fig. 7. For  $T > T^*$ , both the ZF- and LF- $\mu$ SR spectra are well described by a single exponential function, while the fast relaxing component abruptly appears below  $T^*$ . At high temperatures above 100 K, the slow relaxation rate  $\lambda_{\text{s}}$  shows a slight increment with decreasing temperature, indicating that the relaxation is dominated by the exchange fluctuations of the Mn spins. Based on the estimated exchange coupling constant  $J = -3.06$  K from  $\chi_{\text{dc}}(T)$ , we obtain an exchange fluctuation rate  $\nu = \sqrt{2}JS/\hbar \sim 1.6 \times 10^{12} \text{ s}^{-1}$ . Using the relation  $\lambda = 2\Delta^2/\nu$  in the motional narrowing limit,  $\lambda_{\text{s}}(T > 100 \text{ K}) = 0.143 \mu\text{s}^{-1}$  provides a field distribution of  $\Delta/\gamma_{\mu} = 3.98$  kG.

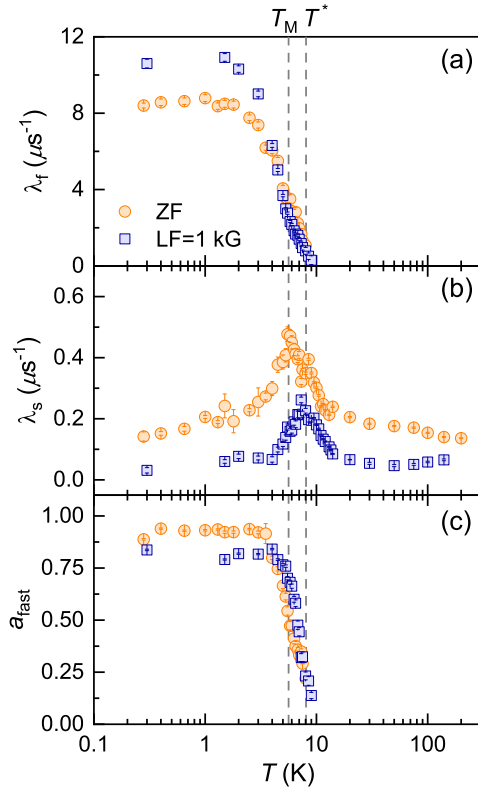


FIG. 7. (a) Temperature dependence of the fast relaxation rate  $\lambda_f$  obtained from the ZF- and LF- $\mu$ SR measurements. (b) Slow muon spin relaxation rate  $\lambda_s$  as a function of temperature. (c) Magnetic volume fraction for the fast relaxing component  $a_{\text{fast}}$  vs temperature. All data are plotted in a semilog scale. The dashed vertical lines indicate the characteristic temperatures  $T_M$  and  $T^*$ .

As shown in Fig. 7(a), the fast relaxation rate  $\lambda_f(T)$  increases steeply through  $T^* = 8$  K and levels off to a nearly constant value below 3 K. Similarly, the fast relaxing fraction  $a_{\text{fast}}(T)$  displays an analogous temperature behavior to  $\lambda_f(T)$  [see Fig. 7(c)]. The temperature evolution of the fast relaxing component is well consistent with the establishment of magnetic correlations at low temperatures. On the other hand, the slow relaxation rate  $\lambda_s(T)$  provides evidence for partially frozen moments [see Fig. 7(b)]. With decreasing temperature below 200 K,  $\lambda_s(T)$  shows a gradual increment. Upon further cooling,  $\lambda_s(T)$  increases steeply through 15 K and exhibits a  $\lambda$ -like anomaly around  $T_M \sim 6$  K, slightly below  $T^* = 8$  K. The temperature dependence of the slow relaxation rate suggests a critical-like slowing down of spin fluctuations below 15 K and the onset of a nearly frozen spin state below  $T^*$ .

It should be noted that we observe no clear signature for the cooperative paramagnetic-to-paramagnetic crossover through  $|\Theta_{\text{CW}}|$  in the  $\mu$ SR results. A subtle but gradual increment of  $\lambda_s(T)$  upon cooling below 50 K could be related to the crossover behavior.

#### IV. DISCUSSION AND CONCLUSION

By employing multiple thermodynamic and magnetic resonance techniques, we have extracted information about the

temporal and thermal structures of spin correlations in the newly discovered  $S = 2$  KHAFM  $\text{CsMn}_3\text{F}_6(\text{SeO}_3)_2$ . The ac susceptibility,  $\mu$ SR, and ESR techniques enable us to probe the electronic spin fluctuations in a wide range of timescales ( $10^2$ – $10^{10}$  Hz). We could identify two crossover temperatures  $T^* = 8$  K and  $T = |\Theta_{\text{CW}}| \approx 49$  K, which result in three different regimes. The CW temperature provides the effective exchange energy, which distinguishes the paramagnetic from the crossover regimes. Upon cooling through the second crossover  $T^* = 8$  K, the system enters a quasistatic ordered state.

In the paramagnetic regime, both the ac magnetic susceptibility and the P2 line of the ESR signal follow power-law behaviors  $\chi'_{\text{ac}}(T) \sim T^{-0.56(1)}$  and  $\Delta H_{\text{pp}}^{\text{P2}}(T) \sim T^{-0.25(2)}$ , respectively. The power-law dependence observed at long- and short-time windows would signify short-range spin-spin correlations. Such a critical power-law dependence of physical quantities, including dc magnetic susceptibility, ESR linewidth, and muon spin relaxation rate, has been reported in a series of low-dimensional frustrated magnets that show short-range order [44–47].

In the cooperative paramagnetic (classical spin liquid) regime,  $C_m(T)$  shows that a short-range order at  $T_{\text{cl}}$  and  $\Delta S_m$  is released below  $T = |\Theta_{\text{CW}}|$ .  $\Delta H_{\text{pp}}^{\text{P1}}(T)$  parallels  $C_m(T)$  in its temperature evolution, showing a broad maximum at  $T_{\text{cl}}$ . In sharp contrast, the P2 component undergoes a critical-like broadening  $\Delta H_{\text{pp}}^{\text{P2}}(T) \sim T^{-1.32(1)}$  and eventually wipes out at about  $T \approx T_{\text{cl}}$ . The dichotomic spin correlations are consistent with a distribution of timescales predicted by the theoretical calculations [16]. Since the breathing anisotropy is negligibly small, it is less probable that the observed two different timescales of spin fluctuations pertain to the breathing distortion.

At low temperatures below  $T^*$ , thermodynamic evidence for broken continuous symmetries is lacking. The ac magnetic susceptibility and the linewidth of the P1 ESR signal show power-law dependences  $\chi'_{\text{ac}}(T) \sim T^{-0.19(1)}$  and  $\Delta H_{\text{pp}}^{\text{P1}}(T) \sim T^{-1.03(8)}$ . Only the  $\mu$ SR data evidence the presence of partially frozen moments based on the  $\lambda$ -like anomaly of  $\lambda_s(T)$  at  $T_M = 6$  K, while the fast component showing up below  $T^*$  reveals the dynamic nature of the ground state. Taken together, the ground state comprises a coexisting quasistatic magnetic order with a coplanar short-range order. The latter is expected in the coplanar regime of the KHAFM.

Lastly, we compare the spin fluctuations in the classical spin liquid phase between  $S = 5/2$  and 2 KHAFMs. A recent  $^{31}\text{P}$  NMR study of the  $S = 5/2$  KHAFM  $\text{Li}_9\text{Fe}_3(\text{P}_2\text{O}_7)_3(\text{PO}_4)_2$  reveals a classical spin-liquid state for  $0.2 < T/|J_{\text{cl}}| < 0.6$  with anisotropic short-range spin correlations, alluding to the persistent nematic correlations or quasistatic magnetic order [19]. On the other hand,  $\text{CsMn}_3\text{F}_6(\text{SeO}_3)_2$  exhibits a timescale distribution of spin correlations in the cooperative paramagnetic regime for  $0.44 < T/|J_{\text{cl}}| < 2.72$ . This feature gives an indication of a cooperative spin liquid, awaiting ultimate confirmation by NMR and inelastic neutron scattering measurements. In particular, it should be clarified whether impurities and Dzyaloshinskii-Moriya interaction present in the studied compound eventually modify the nature of low-energy excitations.

To conclude, we have investigated the temporal and thermal behaviors of spin correlations in the  $S = 2$  KHAFM  $\text{CsMn}_3\text{F}_6(\text{SeO}_3)_2$ . We identify three distinct regimes, consistent with a classical KHAFM system. The timescale-dependent spin dynamics and two distinct spin correlations in the cooperative paramagnetic regime support the notion of timescale distribution inherent to KHAFM. Thus,  $\text{CsMn}_3\text{F}_6(\text{SeO}_3)_2$  can offer new avenues to test theoretical predictions in a KHAFM, including a  $\sqrt{3} \times \sqrt{3}$  ground state and dipolelike correlations.

## ACKNOWLEDGMENTS

The work at SKKU was supported by the National Research Foundation (NRF) of Korea (Grants No. 2020R1A2C3012367 and No. 2020R1A5A1016518). The authors at JUST acknowledge support from the National Natural Science Foundation of China (No. 21671185). Y.O. acknowledges the support from JSPS KAKENHI Grant No. JP19K06606.

- 
- [1] P. Lecheminant, B. Bernu, C. Lhuillier, L. Pierre, and P. Sindzingre, *Phys. Rev. B* **56**, 2521 (1997).
- [2] L. Balents, *Nature* **464**, 199 (2010).
- [3] J. Carrasquilla, Z. Hao, and R. G. Melko, *Nat. Commun.* **6**, 7421 (2015).
- [4] T.-H. Han, J. S. Helton, S. Chu, D. G. Nocera, J. A. Rodriguez-Rivera, C. Broholm, and Y. S. Lee, *Nature (London)* **492**, 406 (2012).
- [5] Y. Zhou, K. Kanoda, and T.-K. Ng, *Rev. Mod. Phys.* **89**, 025003 (2017).
- [6] P. Mendels, F. Bert, M. A. de Vries, A. Olariu, A. Harrison, F. Duc, J. C. Trombe, J. S. Lord, A. Amato, and C. Baines, *Phys. Rev. Lett.* **98**, 077204 (2007).
- [7] B. Fåk, E. Kermarrec, L. Messio, B. Bernu, C. Lhuillier, F. Bert, P. Mendels, B. Koteswararao, F. Bouquet, J. Ollivier, A. D. Hillier, A. Amato, R. H. Colman, and A. S. Wills, *Phys. Rev. Lett.* **109**, 037208 (2012).
- [8] Y. Fu, M.-L. Lin, L. Wang, Q. Liu, L. Huang, W. Jiang, Z. Hao, C. Liu, H. Zhang, X. Shi, J. Zhang, J. Dai, D. Yu, F. Ye, P. A. Lee, P.-H. Tan, and J.-W. Mei, *Nat. Commun.* **12**, 3048 (2021).
- [9] S. Sachdev, *Phys. Rev. B* **45**, 12377 (1992).
- [10] H. T. Diep, *Frustrated Spin Systems* (World Scientific, Singapore, 2004).
- [11] D. A. Garanin and B. Canals, *Phys. Rev. B* **59**, 443 (1999).
- [12] D. A. Huse and A. D. Rutenberg, *Phys. Rev. B* **45**, 7536(R) (1992).
- [13] J. T. Chalker, P. C. W. Holdsworth, and E. F. Shender, *Phys. Rev. Lett.* **68**, 855 (1992).
- [14] C. L. Henley, *Phys. Rev. Lett.* **62**, 2056 (1989).
- [15] I. Ritchev, P. Chandra, and P. Coleman, *Phys. Rev. B* **47**, 15342 (1993).
- [16] M. Taillefumier, J. Robert, C. L. Henley, R. Moessner, and B. Canals, *Phys. Rev. B* **90**, 064419 (2014).
- [17] A. S. Wills, A. Harrison, C. Ritter, and R. I. Smith, *Phys. Rev. B* **61**, 6156 (2000).
- [18] A. Keren, K. Kojima, L. P. Le, G. M. Luke, W. D. Wu, Y. J. Uemura, M. Takano, H. Dabkowska, and M. J. P. Gingras, *Phys. Rev. B* **53**, 6451 (1996).
- [19] E. Kermarrec, R. Kumar, G. Bernard, R. Hénaff, P. Mendels, F. Bert, P. L. Paulose, B. K. Hazra, and B. Koteswararao, *Phys. Rev. Lett.* **127**, 157202 (2021).
- [20] S.-H. Lee, C. Broholm, M. F. Collins, L. Heller, A. P. Ramirez, Ch. Kloc, E. Bucher, R. W. Erwin, and N. Lacey, *Phys. Rev. B* **56**, 8091 (1997).
- [21] X. Obradors, A. Labarta, A. Isalgué, J. Tejada, J. Rodriguez, and M. Pernet, *Solid State Commun.* **65**, 189 (1988).
- [22] Y. J. Uemura, A. Keren, K. Kojima, L. P. Le, G. M. Luke, W. D. Wu, Y. Ajiro, T. Asano, Y. Kuriyama, M. Mekata, H. Kikuchi, and K. Kakurai, *Phys. Rev. Lett.* **73**, 3306 (1994).
- [23] L. Palatinus and G. Chapuis, *J. Appl. Crystallogr.* **40**, 786 (2007).
- [24] V. Petricek, M. Dusek, and L. Palatinus, *Z. Kristallogr.* **229**, 345 (2014).
- [25] J. Jiang, B. Zhu, T. Zhu, H. Yang, Y. Jin, and M. Lü, *Dalton Trans.* **49**, 841 (2020).
- [26] M. Lü, J. Jiang, B. Zhu, Y. Zhao, T. Zhu, H. Yang, Y. Jin, H. Kabbour, K.-Y. Choi, and W. T. A. Harrison, *Dalton Trans.* **49**, 2234 (2020).
- [27] J. Jiang, S. Lee, B. Zhu, Y. Yu, J. C. Waerenborgh, K.-Y. Choi, and M. Lü, *Inorg. Chem.* **58**, 133 (2019).
- [28] See Supplemental Material at <http://link.aps.org/supplemental/10.1103/PhysRevB.105.094439> for the structural details and basic characterizations.
- [29] A. Suter and B. M. Wojek, *Phys. Proc.* **30**, 69 (2012).
- [30] R. Moessner, *Can. J. Phys.* **79**, 1283 (2001).
- [31] M. E. Zhitomirsky, *J. Phys.: Conf. Ser.* **592**, 012110 (2015).
- [32] H. Nakano and T. Sakai, *J. Phys. Soc. Jpn.* **84**, 063705 (2015).
- [33] B. Koteswararao, R. Kumar, J. Chakraborty, B.-G. Jeon, A. V. Mahajan, I. Dasgupta, K. H. Kim, and F. C. Chou, *J. Condens. Matter Phys.* **25**, 336003 (2013).
- [34] B. Koteswararao, S. K. Panda, R. Kumar, K. Yoo, A. V. Mahajan, I. Dasgupta, B. H. Chen, K. H. Kim, and F. C. Chou, *J. Condens. Matter Phys.* **27**, 426001 (2015).
- [35] S.-S. Lee and P. A. Lee, *Phys. Rev. Lett.* **95**, 036403 (2005).
- [36] J. S. Helton, K. Matan, M. P. Shores, E. A. Nytko, B. M. Bartlett, Y. Yoshida, Y. Takano, A. Suslov, Y. Qiu, J.-H. Chung, D. G. Nocera, and Y. S. Lee, *Phys. Rev. Lett.* **98**, 107204 (2007).
- [37] A. Zorko, M. Pregelj, M. Klanjšek, M. Gomilšek, Z. Jagličić, J. S. Lord, J. A. T. Verezhak, T. Shang, W. Sun, and J.-X. Mi, *Phys. Rev. B* **99**, 214441 (2019).
- [38] R. W. Smaha, W. He, J. M. Jiang, J. Wen, Y.-F. Jiang, J. P. Sheckelton, C. J. Titus, S. G. Wang, Y.-S. Chen, S. J. Teat, A. A. Aczel, Y. Zhao, G. Xu, J. W. Lynn, H.-C. Jiang, and Y. S. Lee, *npj Quantum Mater.* **5**, 23 (2020).
- [39] S. Lee, S.-H. Do, W. Lee, Y. S. Choi, J. van Tol, A. P. Reyes, D. Gorbunov, and W.-T. Chen, and K.-Y. Cho, *npj Quantum Mater.* **6**, 47 (2021).
- [40] A. Yaouanc and P. Dalmas de Rotier, *Muon Spin Rotation, Relaxation, and Resonance: Applications to Condensed Matter* (Oxford University Press, Oxford, 2011).
- [41] K. Tustain, B. Ward-O'Brien, F. Bert, T. Han, H. Luetkens, T. Lancaster, B. M. Huddart, P. J. Baker, and L. Clark, *npj Quantum Mater.* **5**, 74 (2020).



- [42] J. Sugiyama, H. Nozaki, M. Harada, K. Kamazawa, Y. Ikedo, Y. Miyake, O. Ofer, M. Månsson, E. J. Ansaldo, K. H. Chow, G. Kobayashi, and R. Kanno, *Phys. Rev. B* **85**, 054111 (2012).
- [43] L. Marcipar, O. Ofer, A. Keren, E. A. Nytko, D. G. Nocera, Y. S. Lee, J. S. Helton, and C. Bains, *Phys. Rev. B* **80**, 132402 (2009).
- [44] S.-H. Do, W.-J. Lee, S. Lee, Y. S. Choi, K.-J. Lee, D. I. Gorbunov, J. Wosnitza, B. J. Suh, and K.-Y. Choi, *Phys. Rev. B* **98**, 014407 (2018).
- [45] S. T. Rodan, S. Yoon, S. Lee, K.-Y. Choi, G. Kim, J.-S. Rhyee, A. Koda, W.-T. Chen, and F. Chou, *Phys. Rev. B* **98**, 214412 (2018).
- [46] S. Yoon, W. Lee, S. Lee, J. Park, C. H. Lee, Y. S. Choi, S.-H. Do, W.-J. Choi, W.-T. Chen, F. Chou, D. I. Gorbunov, Y. Oshima, A. Ali, Y. Singh, A. Berlie, I. Watanabe, and K.-Y. Choi, *Phys. Rev. Materials* **5**, 014411 (2021).
- [47] H. Yamaguchi, S. Kimura, M. Hagiwara, Y. Nambu, S. Nakatsuji, Y. Maeno, and K. Kindo, *Phys. Rev. B* **78**, 180404(R) (2008).